The photo-orientation of azobenzene in viscous solutions, simulated by a stochastic model.

Valentina Cantatore, Giovanni Granucci, Maurizio Persico,

Dipartimento di Chimica e Chimica Industriale, Università di Pisa,

v. G. Moruzzi, I-56124 Pisa, Italy

Correspondence to: Valentina Cantatore, e-mail: valecantatore@yahoo.it

Abstract We report a computational study of the photo-orientation kinetics in a viscous solution of azobenzene in ethylene glycol, under irradiation with linearly polarized light. The development of anisotropy and its interplay with photoisomerization are simulated by a stochastic model. A distinctive feature of the model is that it takes into account the photo-orientation angular distributions, specific for each isomer, obtained by nonadiabatic dynamics simulations at molecular level. We find that the anisotropy, as measured by optical absorption dichroism, does not necessarily increase monotonously in time. As expected, the photo-orientation turns out to be strongly coupled with photoisomerization, but the latter is not a mandatory ingredient of this phenomenon: we predict that any chromophore undergoing large amplitude geometry relaxation during its excited state dynamics can develop anisotropy in suitable conditions.

Keywords: Azobenzene - Photo-orientation - Photoisomerization - Optical anisotropy - Stochastic simulations

1   Introduction

The development of anisotropy under irradiation with polarized light occurs in materials containing suitable chromophores, and in particular azobenzene and its derivatives [1–13]. The phenomenon of photo-orientation is of potential interest for technological applications, especially in materials where the chromophores do interact with each other, so that a phase with some degree of orientational order is stabilized, as in liquid crystals. In this paper we investigate a much simpler situation, in which the azobenzene molecules form a dilute solution in a viscous solvent. Nevertheless, the detailed simulation of the photo-orientation process, even in the absence of interactions between the chromophores, reveals non trivial aspects mainly related to the interplay of photoisomerization and photo-orientation.

The simulations we present are based on the stochastic model described in a previous paper [14] and shortly outlined in section 2. The model makes use of rotational diffusion data computed by molecular dynamics in the ground state, and of angular distributions that describe the reorientation of *trans* and *cis*-azobenzene (TAB and CAB, respectively), when they undergo a photocycle, i.e. excitation and decay to the ground state with or without isomerization. The latter data were extracted from nonadiabatic dynamics simulations, run with the surface hopping method, concerning the $\pi \to \pi^*$ excitation of azobenzene [15]. Potential energy surfaces (PES) and wavefunctions were obtained on the fly by the semiempirical FOMO-CI method, specifically parameterized to this aim [16]. To the best of our knowledge, this is the first approach to the photo-orientation problem that relies on angular distributions computed in detail by molecular dynamics, rather than assuming simplified models with parameters that can be empirically adjusted [17–21]. While our procedure consists of two steps, first the single chromophore dynamics, then the photoisomerization and photo-orientation kinetics, a single-step strategy was proposed by Doltsinis and coworkers to simulate the behavior of mesogenic azo-compounds [22]. In their approach, for most of the time the system is described by atomistic or even coarse grained Molecular Dynamics, but upon photon absorption a chromophore is temporarily promoted to the status of quantum mechanical subsystem in a QM/MM treatment. An important advantage of this procedure is that the interactions between chromophores can be accounted for. On the other hand, our method is less computer intensive and allows to obtain a better statistics (large molecular samples and many

photochemical cycles) and to perform longer simulations.

In section 3 we shall comment upon the rotational diffusion data and how they are affected by the internal dynamics of azobenzene. The photochemical reorientation results and their relationship with photoisomerization are presented in section 4. Section 5 describes two kinds of simulated experiments, one with long light pulses that allow to reach the photostationary state, and one with 100 ps pulses, followed by relaxation towards the isotropic state.

2   Model and computational details

Here we shortly outline the stochastic model we apply in this work; for a detailed description, we refer the reader to a previous paper [14]. We consider a large set of molecules labelled m, each characterized by its time-dependent orientation $\Omega_m(t)$, i.e. by the three Euler angles α_m, β_m and γ_m [23]. The molecular frame $\hat{x}, \hat{y}, \hat{z}$, connected to the laboratory frame $\hat{X}, \hat{Y}, \hat{Z}$ by the rotation Ω_m, is defined by a rule that applies to the equilibrium structures of the two isomers as well as to any intermediate and non symmetric geometry (see Fig. 1 and Appendix A). Only the azo-group C′N′N″C″ atoms are taken into account in defining the molecular axes. The nitrogen atoms lie on the $\hat{x}$ axis and, at C_2 or C_{2h} geometries, the $\hat{z}$ axis always coincides with the

Figure 1: *trans* and *cis*-azobenzene (TAB and CAB), the associated molecular frames and the $\pi \rightarrow \pi^*$ transition dipole moments.
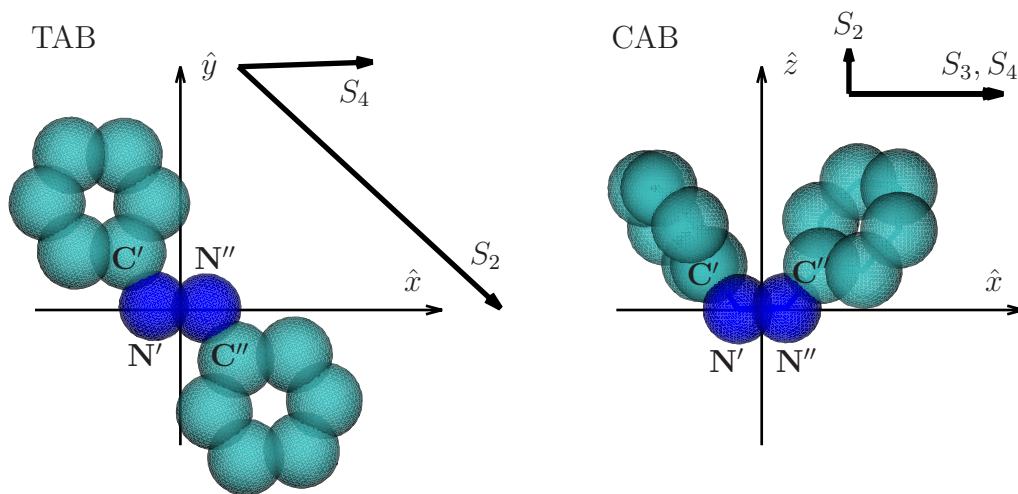
Table 1: Transition energies $\Delta E_{0,n}$ (eV) and dipole moments $\vec{\mu}_{0,n}$ (a.u.) for the $S_0 \to S_n$ absorption of *trans* and *cis*-azobenzene in vacuo, obtained by FOMO-CI [16] at the ground state equilibrium geometries.

	TAB				CAB			
n	$\Delta E_{0,n}$	$\mu_{0,n,x}$	$\mu_{0,n,y}$	$\mu_{0,n,z}$	$\Delta E_{0,n}$	$\mu_{0,n,x}$	$\mu_{0,n,y}$	$\mu_{0,n,z}$
1	2.83	0.00	0.00	0.00	2.89	-0.31	0.42	0.00
2	4.04	2.34	2.36	0.00	4.59	0.00	0.00	0.43
3	4.22	0.00	0.00	0.00	4.88	1.39	-0.49	0.00
4	4.24	1.21	-0.04	0.00	4.98	1.35	0.59	0.00

symmetry axis.

The modules and directions of the transition dipole moments are such that the polarization of the strongest transitions is practically parallel to the line joining the two *para* carbon atoms in both isomers, i.e. to the longer axis of inertia in TAB and to the N=N bond in CAB, as shown in Table 1 and Fig. 1 (however, in CAB the $S_0 \to S_3$ and $S_0 \to S_4$ transitions also have minor components along the $\hat{y}$ axis).

At the beginning of the simulation ($t = 0$) the molecular orientations Ω_m are distributed isotropically. All molecules are in the ground state and undergo rotational diffusion. The rotational diffusion data were extracted from a long thermal trajectory for each isomer of azobenzene in ethylene glycol, a moderately viscous solvent, at 300 K [14] (see next section for a discussion on the mobility of azobenzene in the solvent cage). The data were put in the form of two $\Omega_{rd,I}$ time sequences, describing the thermal reorientation of each isomer I (I = TAB or CAB) in the ground state. At $t = 0$, for each molecule m we pick up at random a time t_0 along the thermal trajectory and we propagate the orientation $\Omega_m(t)$ according to the time sequence $\Omega_{rd,I}(t - t_0)$ (here I is the starting isomer).

We model the action of a continuous wave radiation field, linearly polarized along the $\hat{Z}$ axis (laboratory frame). The absorption rate per molecule of isomer I in an isotropic sample is

$$\langle A_I(\lambda) \rangle_{iso} = \frac{1000 \ ln(10) \ \varepsilon_I(\lambda) \ F}{N_A \Delta E(\lambda)} \tag{1}$$

Here λ is the wavelength and F is the irradiance in W/cm^2 of the monochromatic light; $\Delta E = hc/\lambda$ is the photon energy and N_A is Avogadro's number.

The experimental extinction coefficients $\varepsilon_I(\lambda)$ for TAB or CAB are used, to obtain a more accurate dependence of the simulation results on the excitation wavelength λ_{exc}. The excitation probability of a molecule m with orientation Ω_m during the time step Δt is assumed to be:

$$P_{exc}(\Omega_m) = \langle A_I(\lambda_{exc}) \rangle_{iso} \, \frac{3\mu_{m,0,n,Z}^2}{\mu_{m,0,n}^2} \, \Delta t \tag{2}$$

The ratio $\mu_{m,0,n,Z}^2 / \mu_{m,0,n}^2$ takes into account the effect of light polarization. The Z component of the transition dipole $\vec{\mu}_{m,0,n}$ depends on the orientation Ω_m of the molecule. Of course $\vec{\mu}_{m,0,n}$ also depends on the molecular geometry, but the $\pi \to \pi^*$ transition dipoles are not very sensitive to conformational changes, unlike the $n \to \pi^*$ one in TAB [24]. The $\pi \to \pi^*$ band of azobenzene is made of at least three transitions, to S_2, S_3 and S_4, so in our nonadiabatic dynamics simulations each photochemical trajectory starts with a vertical transition to one of these states. The initial state is determined by a sampling procedure, that takes into account the squared transition dipoles [15].

At each time step, we assign the $\vec{\mu}_{m,0,n}$ vector to molecule m, by pre-emptively picking up at random a photochemical trajectory in the database of the appropriate isomer I. We then use the initial transition dipole moment associated with that trajectory to compute the $P_{exc}(\Omega_m)$ probability by eq. (2). If $P_{exc}(\Omega_m)$ turns out to be larger than a random number drawn in the range $[0, 1]$, the molecule m is excited and starts evolving according to the precomputed photodynamics. This affects its orientation, as well as the transition energies and dipole moments. Moreover, during the photochemical trajectory the molecule can go back to the initial isomer I or switch to the other isomer (unreactive or reactive trajectories, respectively). The quantum yields we obtained from the $\pi \to \pi^*$ photodynamics in ethylene glycol [15], i.e. the fractions of reactive trajectories, are $\Phi_{\text{TAB}\to\text{TAB}} = 0.24$ and $\Phi_{\text{CAB}\to\text{TAB}} = 0.55$. The last part of a photochemical trajectory represents the hot ground state dynamics that contributes significantly to the light induced reorientation. In the surface hopping single molecule dynamics each trajectory had a minimum duration, after which it was stopped when two conditions were met: to be in the electronic ground state, and to be geometrically close to the equilibrium structure of one of the two isomers. The duration of most trajectories was between 1 and 3 ps. At the end of a photochemical trajectory the molecule reverts to the rotational diffusion dynamics, by picking up the thermal trajectory of the isomer I or I', as appropriate, at a random time t_0 as done at the

beginning of the simulation.

Summarizing, the whole simulation procedure consists of three parts, the first and second being described in detail in previous papers [15, 25]:

(1) Ground state dynamics, run by a QM/MM representation of azobenzene in a cluster of solvent The force field for the solvent (ethylene glycol) was a modified OPLS [25] and the QM-MM interactions were parameterized on the basis of MP2 calculations [16]. The rotation of the molecular frame during each time step is recorded to build up the rotational diffusion database, which is illustrated in section 3.

(2) Excited state dynamics, run by the same QM/MM approach. State-specific solute-solvent interactions were taken into account by electrostatic embedding [26]. The nonadiabatic dynamics is deeply affected by S_2/S_1 and S_1/S_0 conical intersections [15]. The rotations of the molecular frame computed for several hundreds trajectories starting with each isomer constitute the photo-induced reorientation database, analyzed in section 4.

(3) Photo-orientation and photoisomerization kinetics, computed by the stochastic method described above. Each molecule rotates according to either the rotational diffusion or the photo-induced reorientation database. It switches in time from the former to the latter stochastically, according to the excitation probability that depends on the angle between the transition dipole and the light polarization. Every time a molecule is excited, the photochemical trajectory is picked up at random, so it may or may not involve isomerization. When it ends, the molecule resumes the thermal rotational diffusion.

In this work the number of molecules in the sample was $N_M = 3732480$. The time step was $\Delta t = 0.5$ ps. At every time step we counted the number N_I of molecules belonging to each isomer I and the corresponding fractions $F_I = N_I/N_M$. We also computed the densities $\rho_I(\Omega, t)$ that represent the anisotropy of the molecular orientations for each isomer. Each density is normalized to 1, to facilitate the comparison of ρ_{TAB} and ρ_{CAB}:

$$\int \rho_I(\Omega, t)d\Omega = \int_0^{2\pi} d\alpha \int_0^\pi sin\beta d\beta \int_0^{2\pi} d\gamma \ \rho_I(\alpha, \beta, \gamma, t) = 1 \qquad (3)$$

The reduced densities, functions of α, β or γ only, are more easily represented and interpreted; they are defined as:

$$\rho_{\alpha,I}(\alpha, t) = \int_0^\pi sin\beta d\beta \int_0^{2\pi} d\gamma \ \rho_I(\Omega, t) \qquad (4)$$

$$\rho_{\beta,I}(\beta, t) = \int_0^{2\pi} d\alpha \int_0^{2\pi} d\gamma \ \rho_I(\Omega, t) \tag{5}$$

$$\rho_{\gamma,I}(\gamma, t) = \int_0^{2\pi} d\alpha \int_0^{\pi} sin\beta \ d\beta \ \rho_I(\Omega, t) \tag{6}$$

The computational details can be found in our previous work [14].

The angular distributions offer a complete description of the anisotropy, that may affect structural [3–5, 8, 11, 13], optical [6, 7, 9, 10] or magnetic [4, 12] properties. One of the easiest ways to probe the anisotropy is to measure the optical dichroism. In this work we predict the time evolution of the dichroic ratio

$$R_{tot}(\lambda_{probe}) = \frac{\left\langle A_{\parallel}(\lambda_{probe}) \right\rangle - \left\langle A_{\perp}(\lambda_{probe}) \right\rangle}{\left\langle A_{\parallel}(\lambda_{probe}) \right\rangle + 2 \left\langle A_{\perp}(\lambda_{probe}) \right\rangle} \tag{7}$$

where $\left\langle A_{\parallel}(\lambda_{probe}) \right\rangle$ and $\left\langle A_{\perp}(\lambda_{probe}) \right\rangle$ are the absorbance rates, averaged over the sample, for light of wavelength λ_{probe}, linearly polarized in the same direction as the exciting light, or perpendicular to it, respectively. We compute the dichroic ratio R_I for each isomer I by using an expression similar to eq. (7) and the absorbance rates

$$\left\langle A_{\parallel} \right\rangle_I = \frac{3 \left\langle A_I(\lambda_{probe}) \right\rangle_{iso}}{N_I} \sum_{m \in I} \frac{\mu_{m,0,n,Z}^2}{\mu_{m,0,n}^2} \tag{8}$$

and

$$\left\langle A_{\perp} \right\rangle_I = \frac{3 \left\langle A_I(\lambda_{probe}) \right\rangle_{iso}}{N_I} \sum_{m \in I} \frac{\mu_{m,0,n,X}^2 + \mu_{0,n,Y}^2}{2\mu_{m,0,n}^2} \tag{9}$$

Here the sums run over the molecules m of the isomer I. The state n is chosen according to a mixed resonance and transition strength criterion, i.e. by maximizing the quantity

$$\mu_{m,0,n}^2 \left[1 + \alpha^2 \left(1 - \frac{\Delta E_{m,0,n}}{\Delta E(\lambda_{probe})} \right)^2 \right]^{-1} \tag{10}$$

The parameter α determines the bandwidth and we chose $\alpha = 5$. Since

$$\left\langle A_{\parallel} \right\rangle_I + 2 \left\langle A_{\perp} \right\rangle_I = \left\langle A_I \right\rangle_{iso} \tag{11}$$

6

and

$$\left\langle A_{\parallel} \right\rangle = \sum_{I} F_{I} \left\langle A_{\parallel} \right\rangle_{I}, \qquad \left\langle A_{\perp} \right\rangle = \sum_{I} F_{I} \left\langle A_{\perp} \right\rangle_{I} \qquad (12)$$

the total dichroic ratio is a weighted average of those of the two isomers [27]:

$$R_{tot} = \frac{F_{\text{TAB}} \left\langle A_{\text{TAB}} \right\rangle_{iso} R_{\text{TAB}} + F_{\text{CAB}} \left\langle A_{\text{CAB}} \right\rangle_{iso} R_{\text{CAB}}}{F_{\text{TAB}} \left\langle A_{\text{TAB}} \right\rangle_{iso} + F_{\text{CAB}} \left\langle A_{\text{CAB}} \right\rangle_{iso}} \qquad (13)$$

To simulate the simplest experiment of this kind, that could be performed with a single laser source, in this work we chose $\lambda_{probe} = \lambda_{exc}$.

3   Rotational diffusion.

The rotational diffusion of TAB and CAB presents some peculiar features, that are due at least in part to the internal motions of the two molecules. Of course, all the large amplitude motions, both the internal ones and the overall rotations, take place so as to be minimally hindered by the solvent cage, i.e. without disrupting it. Figure 2 shows the time dependence of the scalar products of each molecular axis at time t with the same axis at time 0, $\hat{n}(t) \cdot \hat{n}(0) \equiv cos\theta_{n}$, where $\theta_{n}(t)$ is the angle between $\hat{n}(t)$ and $\hat{n}(0)$ ($\hat{n} = \hat{x}, \hat{y}$ or $\hat{z}$). In Figures S1 and S2 (Supplementary Information) we plot the autocorrelation functions

$$\left\langle P_{1,n} \right\rangle (t) = \left\langle \hat{n}(t_{0}) \cdot \hat{n}(t_{0} + t) \right\rangle \qquad (14)$$

and

$$\left\langle P_{2,n} \right\rangle (t) = \frac{1}{2} \left\langle 3[\hat{n}(t_{0}) \cdot \hat{n}(t_{0} + t)]^{2} - 1 \right\rangle \qquad (15)$$

Here the average is performed with respect to the starting time t_{0}. In Table 2 we list the parameters of a three-exponential function we use to fit $\left\langle P_{1,n} \right\rangle (t)$ and $\left\langle P_{2,n} \right\rangle (t)$:

$$f(t) = \sum_{i=1}^{3} w_{i} e^{-t/\tau_{i}} \qquad (16)$$

In the fitting we fixed the weights w_{i}, in order to decouple the three time ranges that characterize more or less neatly all the autocorrelation functions we examined. The shortest time τ_{1}, between 0.1 and 0.25 ps, corresponds to

Figure 2: Cosine of the angle θ_n between the molecular axis $\hat{n}(t)$ and the same at $t = 0$, $\hat{n}(0)$ ($\hat{n} = \hat{x}, \hat{y}$ or $\hat{z}$).
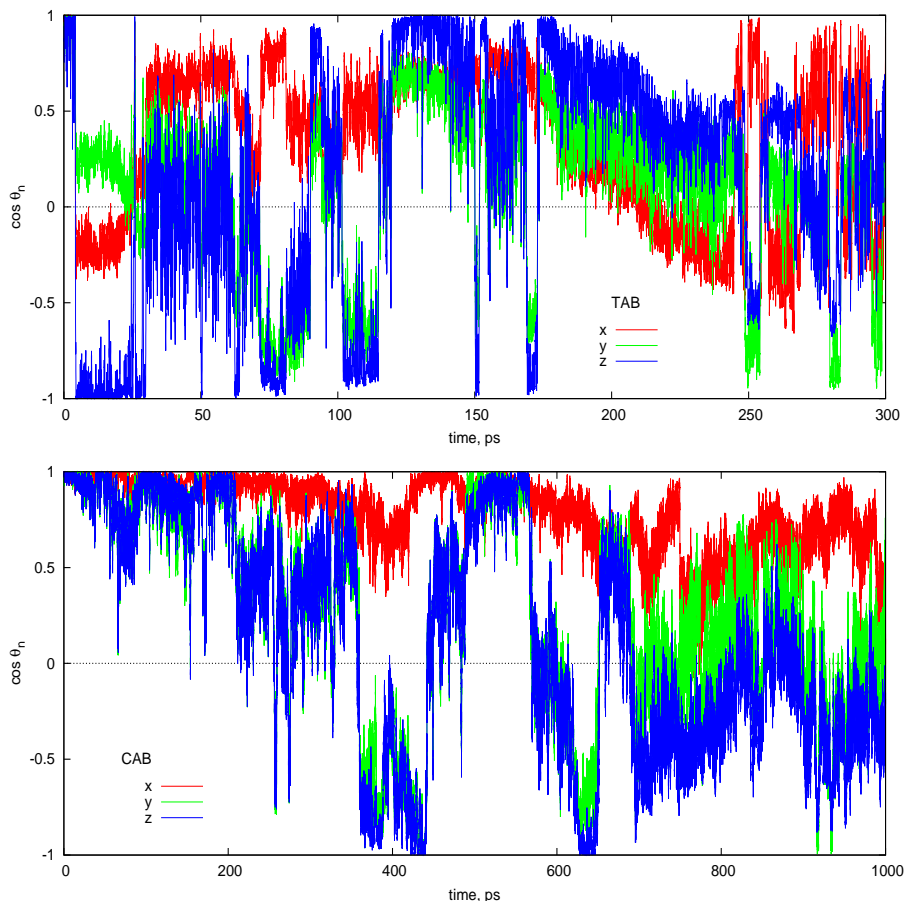
the fast oscillations of the cosines $\hat{n}(t) \cdot \hat{n}(0)$ (Figure 2), that must be related to large amplitude internal modes of azobenzene. τ_1 was graphically adapted to represent the initial drop of the $\langle P_{1,n} \rangle$ and $\langle P_{2,n} \rangle$ values, without optimizing it because of the non-exponential behaviour we found in this time range.

For TAB the observed oscillations in $cos\theta_n$ correspond to frequencies of roughly 100 cm^{-1}. In this range we find the antisymmetric (B_u) NNC bending mode (95 cm^{-1}) and the antisymmetric (B_g) torsion of the N-C bonds, i.e. the "pedalling" motion (113 cm^{-1}). The B_u NNC bending motion affects the orientation of the $\hat{x}$ and $\hat{y}$ axes, while the B_g N-C torsion rotates all three axes. When the pedalling goes as far as half a turn, the $\hat{z}$ axis is reversed, while $\hat{x}$ and $\hat{y}$ rotate by about 90°. This is the reason of the sudden large and simultaneous changes in the three $cos\theta_n$ values. As illustrated in Figure

8

Table 2: Parameters of the three-exponential function, eq. (16), used to fit the $\langle P_{1,n} \rangle$ and $\langle P_{2,n} \rangle$ autocorrelation functions of the molecular axes. Times in ps.

	function	w_1	τ_1	w_2	τ_2	w_3	τ_3
TAB	$\langle P_{1,x} \rangle$	0.08	0.10	0.50	19	0.42	360
TAB	$\langle P_{1,y} \rangle$	0.09	0.10	0.50	16	0.41	320
TAB	$\langle P_{1,z} \rangle$	0.10	0.10	0.60	17	0.40	340
CAB	$\langle P_{1,x} \rangle$	0.04	0.20	0.35	42	0.61	630
CAB	$\langle P_{1,y} \rangle$	0.04	0.20	0.40	39	0.56	510
CAB	$\langle P_{1,z} \rangle$	0.04	0.20	0.40	39	0.56	460
TAB	$\langle P_{2,x} \rangle$	0.20	0.10	0.35	9.2	0.45	80
TAB	$\langle P_{2,y} \rangle$	0.22	0.10	0.36	9.1	0.42	95
TAB	$\langle P_{2,z} \rangle$	0.24	0.10	0.36	10	0.40	63
CAB	$\langle P_{2,x} \rangle$	0.12	0.25	0.60	39	0.28	230
CAB	$\langle P_{2,y} \rangle$	0.12	0.25	0.70	38	0.18	430
CAB	$\langle P_{2,z} \rangle$	0.12	0.25	0.75	41	0.13	620

3, the conversion between the two equivalent conformations of TAB only involves a modest displacement of the N atoms, leaving almost unchanged the orientation of the long axis of the molecule ($\hat{n}_{long}$) because of the constraints imposed by the solvent cage. In this way, the dipole moment relative to the strongest transition ($S_0 \rightarrow S_2$) is almost unaffected by the pedalling motion. The frequent occurrence of such reorientation events determines the τ_2 time constants, that fall in the 10-20 ps range. The longer τ_3 times are probably associated with the slower drift of the orientation of the molecular frame, that is apparent between two pedalling events.

The rotational diffusion of CAB is overall slower than that of TAB. The fast oscillations in the $cos\theta_n(t)$ functions and the initial drop of the autocorrelation functions are less important (compare the insets in Figures S1 and S2). The reason is that the lowest frequency motions (N=N bond torsion, symmetric C-N torsion and NNC symmetric bending) have little effect on the orientation of the molecular axes. The symmetric torsion of the C-N bonds converts the two enantiomeric forms of CAB into each other with small displacements of the azo-group atoms C′N′N″C″, as shown in Figure 3. Apparently the motion most compatible with the solvent cage is an overall rotation around an axis $\hat{n}_{ph-ph}$ roughly parallel to $\hat{x}$ but closer to the center-of-mass of the molecule and going through both phenyl rings (see again Figure 3). This rotation affects

the direction of the $\hat{y}$ and $\hat{z}$ axes, but is less frequent than the TAB pedalling events (compare the two panels of Figure 2, being aware of the different time scales). These observations explain why all the time constants of CAB, shown in Table 2, are longer than the corresponding ones of TAB.

Figure 3: Internal motions and overall rotations of TAB and CAB.

TAB pedalling

CAB enantiomerization

CAB rotation
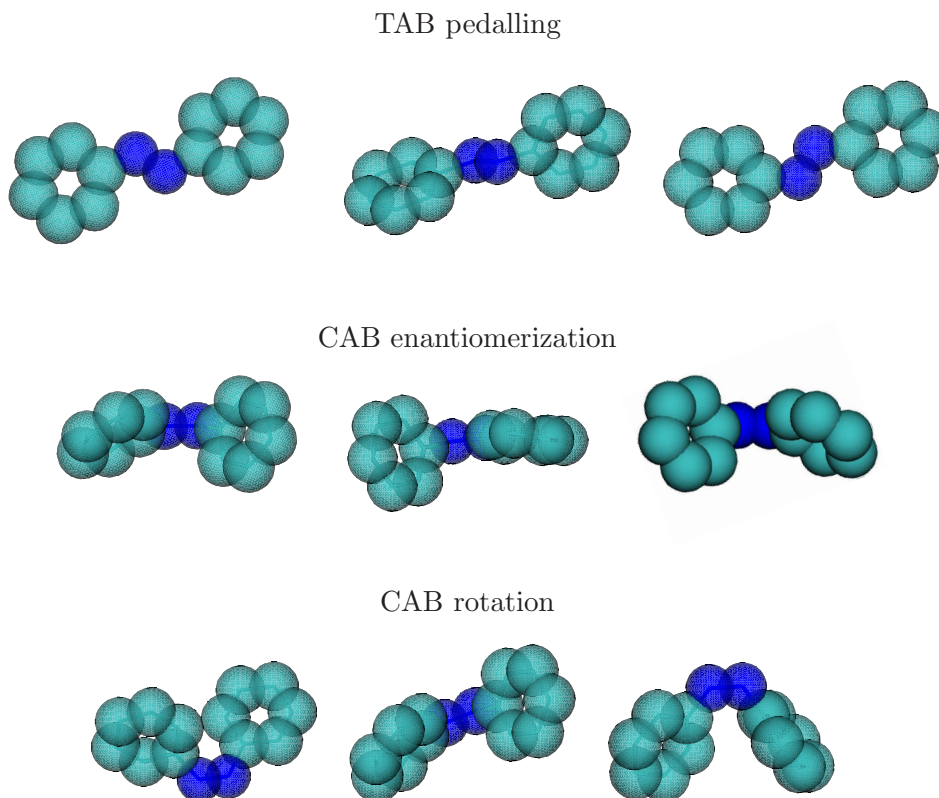
4 Photo-orientation angular distributions.

The photo-orientation data employed in the present simulations were drawn from our previous study on the $\pi \rightarrow \pi^*$ photodynamics in ethylene glycol [15]. In that work we examined the mechanism of excited state decay and photoisomerization in vacuo and in solution. As observed in section 3 with regard to the rotational diffusion, also the photoinduced large amplitude motions take place are somehow hindered and limited by the solvent cage. For instance, the $trans \rightarrow cis$ photoisomerization mechanism is essentially a torsion of the N=N double bond, assisted by concerted torsions of the N-C bonds in order

Table 3: Autocorrelation functions $\langle P_{1,n}\rangle(t)$ and $\langle P_{2,n}\rangle(t)$ of the molecular axes, according to eqs. (14) and (15), as in the thermal case. With t=final we indicate the same functions computed for the final molecular frame of each trajectory. For comparison we also list the values of the autocorrelation functions for the thermal trajectories at $t = 1$ and $t = 2$ ps.

kind of trajectories	t (ps)	$\langle P_{1,x}\rangle$	$\langle P_{1,y}\rangle$	$\langle P_{1,z}\rangle$	$\langle P_{2,x}\rangle$	$\langle P_{2,y}\rangle$	$\langle P_{2,z}\rangle$
TAB excitation, reactive	1	0.66	-0.16	-0.31	0.21	0.09	0.49
TAB excitation, unreactive	1	0.63	0.74	0.39	0.33	0.45	0.41
TAB excitation, all trajs.	1	0.63	0.53	0.22	0.31	0.3	0.43
TAB excitation, reactive	final	0.61	-0.31	-0.44	0.09	-0.11	0.35
TAB excitation, unreactive	final	0.61	0.75	0.38	0.32	0.45	0.40
TAB excitation, all trajs.	final	0.61	0.49	0.18	0.27	0.32	0.39
TAB, thermal	1	0.87	0.86	0.84	0.74	0.72	0.70
TAB, thermal	2	0.83	0.81	0.79	0.69	0.68	0.65
CAB excitation, reactive	1	0.65	-0.03	-0.08	0.16	-0.14	0.26
CAB excitation, unreactive	1	0.95	0.79	0.81	0.86	0.66	0.73
CAB excitation, all trajs.	1	0.78	0.34	0.32	0.47	0.22	0.47
CAB excitation, reactive	final	0.62	-0.04	-0.11	0.10	-0.19	0.24
CAB excitation, unreactive	final	0.97	0.86	0.87	0.92	0.71	0.73
CAB excitation, all trajs.	final	0.78	0.36	0.33	0.47	0.21	0.46
CAB, thermal	1	0.95	0.95	0.95	0.87	0.86	0.86
CAB, thermal	2	0.94	0.94	0.94	0.84	0.83	0.83

to displace as little as possible the phenyl groups. Such solvent imposed constraints determine the reorientation of the molecular frame during a cycle of photoexcitation and decay to the ground state, with or without isomerization. Figure 4 shows the distribution of reorientations obtained by comparing the initial and the final molecular frame for all the photochemical trajectories (619 starting from excited TAB and 557 from CAB). At the beginning of each trajectory the molecular axes conventionally coincide with the lab ones. For each molecular axis we show the components it has eventually acquired along the two other laboratory axes (Y and Z for $\hat{x}$ and so on), using a red dot if the trajectory is reactive, or a blue one if it is unreactive.

In Table 3 we list the values of the autocorrelation functions $\langle P_{1,n}\rangle(t)$ and $\langle P_{2,n}\rangle(t)$ of the molecular axes along the photochemical trajectories, defined by eqs. (14) and (15), with $t = 1$ ps. The only difference with respect to

Figure 4: Rotation of the molecular frame due to a photochemical event (photon absorption and decay to the ground state, with or without isomerization). Each dot represents two components of a molecular axis at the end of a photochemical trajectory (the initial molecular frame coincides with the lab frame). The label in the top right corner of each panel indicates the molecular axis. Red and blue dots indicate reactive and unreactive trajectories, respectively.
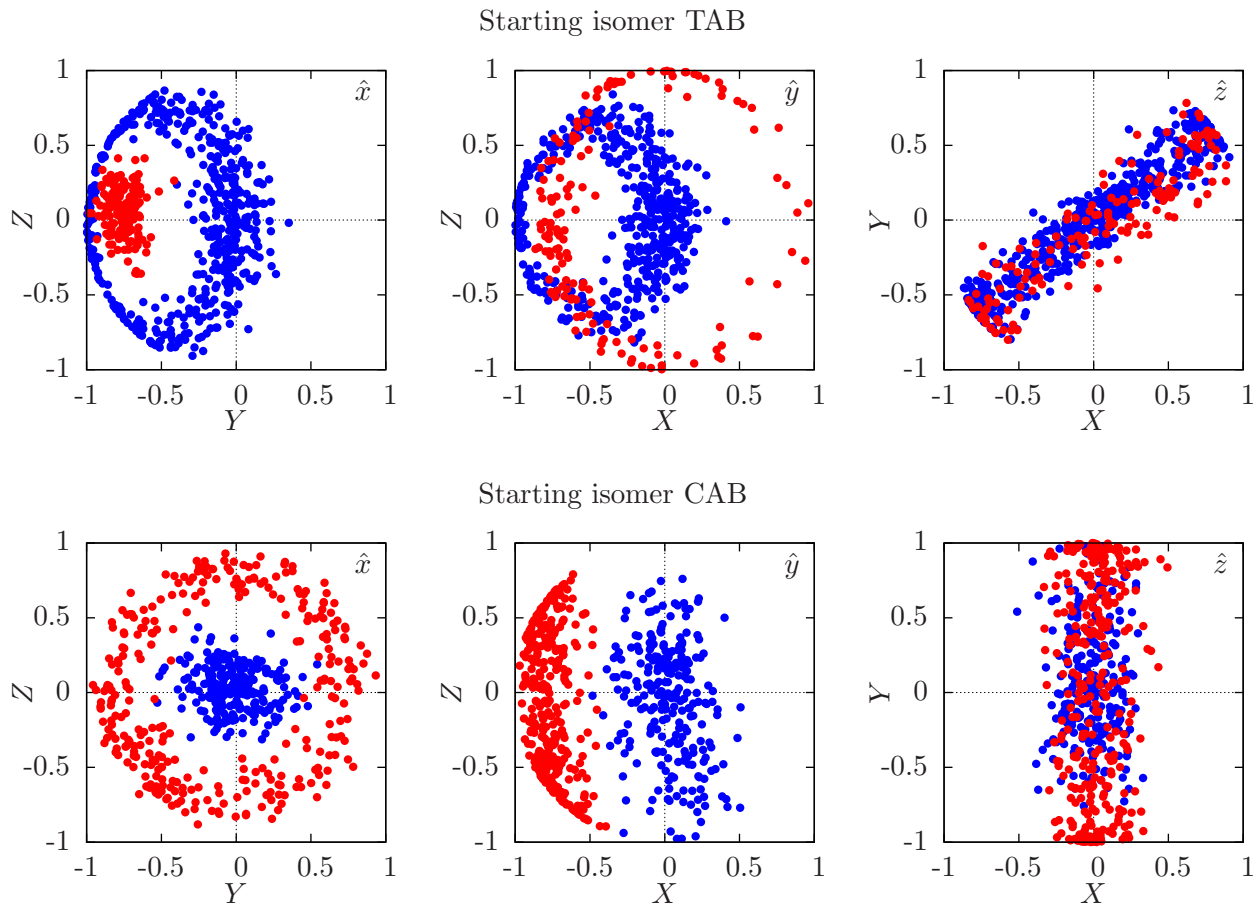
ground state rotational diffusion is that we also compute the averages of data concerning the final times of all trajectories. Since the average length of a trajectory is 1.28 ps for TAB and 1.35 for CAB, we list for comparison the values of the autocorrelation functions of the thermal trajectories at $t = 1$ and $t = 2$ ps. The higher autocorrelation values obtained for the thermal dynamics, even at $t = 2$ ps, confirm that the photocycle is much more effective in reorienting the molecular frame than an equivalent time spent in the ground state at 300 K. From Table 3 and from Figure 4 we also see that the reactive trajectories are more effective than the unreactive ones, with the notable exception of the

$\hat{x}$ axis of TAB.

Inspection of the upper panels of Figure 4 shows that the simplest reorientation of the molecular frame caused by TAB excitation concerns the unreactive trajectories, and is a rotation around the long axis of the molecule, $\hat{n}_{long}$. Since the $\hat{x}$ and $\hat{y}$ axes make angles of about 45° with $\hat{n}_{long}$, they describe cones in space, that correspond to annular distributions of blue dots. The $\hat{z}$ axis is instead perpendicular to $\hat{n}_{long}$, so it rotates approximately in a plane and yields a "diagonal" distribution, with dots close to the bisectors of the I and III quadrants. Similarly, the unreactive events promote the rotation of CAB around the $\hat{n}_{ph-ph}$ axis roughly parallel to $\hat{x}$, so the latter is relatively unaffected, while $\hat{y}$ acquires a Z component and $\hat{z}$ a Y one. All these distributions show the maximum density of dots around the center of the diagram (no rotation). On the contrary, the reactive trajectories produce some well-defined reorientations. In the $trans \rightarrow cis$ conversion, the double bond torsion pulls the two N atoms in opposite directions along the $\hat{Y}$ axis, so the N-N axis, i.e. $\hat{x}$, acquires a negative Y component; at the same time, a rotation of the whole molecule can take place, similarly to the unreactive case, around the $\hat{n}_{long}$ axis of the starting isomer TAB or the $\hat{n}_{ph-ph}$ axis of the final isomer CAB (note that the two axes are practically parallel): this produces the annular distribution of red dots in the $\hat{y}$ diagram, and the diagonal one in the $\hat{z}$ diagram. Finally, the $cis \rightarrow trans$ photoisomerization too initially displaces the $\hat{x}$ and $\hat{y}$ axes so that $\hat{x}$ acquires a positive Y component and $\hat{y}$ a negative X component; in addition, an overall rotation occurs about the long axis of the TAB reaction product, i.e. essentially about the lab axis $\hat{X}$, so both $\hat{x}$ and $\hat{y}$ describe cones in space, that appear as a ring in the $\hat{x}$ diagram and a crescent in the $\hat{y}$ one; $\hat{z}$ instead rotates in the YZ plane, so the red dots make a vertical band in the corresponding diagram.

The data of Table 3 and of Figure 4 describe in detail the photo-orientation of azobenzene in three dimensions, i.e. a structural information which is related with the change in the direction of the transition dipoles. However, to interpret the development of the optical anisotropy, it is preferable to consider a set of data directly concerning the transition moments themselves. Thus, we computed the vector autocorrelation values

$$\langle P_{2,\mu} \rangle = \frac{1}{2} \left[3 \left\langle \frac{\left(\vec{\mu}^{(i)} \cdot \vec{\mu}^{(f)} \right)^2}{\left(\mu^{(i)} \right)^2 \left(\mu^{(f)} \right)^2} \right\rangle - 1 \right] \tag{17}$$

Here the average is taken over the reactive or the unreactive trajectories, separately. $\vec{\mu}^{(i)}$ is the transition moment concerning the initial excitation for a given trajectory, which is set once for all by the sampling procedure for the initial conditions [15]. $\vec{\mu}^{(f)}$ is one of the $S_0 \rightarrow S_n$ transition moments at the end of the trajectory. If the trajectory is unreactive, S_n is the same state as at the beginning, otherwise we choose the transition with the largest $\left(\mu^{(f)}\right)^2$. In this way we average over the initial-to-final scalar products of the transition moment versors, with weights proportional to the squared modules of the final vectors $\left(\mu_{0,n}^{(f)}\right)^2$.

The computed data are: for TAB excitation, reactive events, $\langle P_{2,\mu} \rangle = 0.17$, and unreactive events, 0.76; for CAB excitation, reactive, 0.22, and unreactive, 0.57. The positive sign of these values indicates a prevalence of conservation of the initial orientation of the polarization, even when photoisomerization occurs. If we compare the dipole autocorrelation data $\langle P_{2,\mu} \rangle$ for unreactive trajectories with the final $\langle P_{2,n} \rangle$ values of Table 3, we see that in the TAB case the autocorrelation of the transition dipole vectors is larger than that of the molecular axes: this is due to the fact that the largest transition dipole is parallel to the long axis of the molecule. For CAB, the dipole autocorrelation is instead smaller than the structural one, probably because we average over three transitions of similar importance but different polarizations. For the reactive trajectories the dipole autocorrelation values are slightly higher than the average of $\langle P_{2,n} \rangle$ over the three axes, for both TAB and CAB.

5 Simulations of the photo-orientation kinetics.

We performed two kinds of simulated experiments, one with a short pulse (100 ps) and one with a much longer one, such as to reach the photostationary state. The standard irradiance was $F = 10$ Gw/cm^2, but we also ran some tests with different values of F. Within the $\pi \rightarrow \pi^*$ bands (250-330 nm) the molar extinction coefficients ε_{TAB} and ε_{CAB} show large variations, and even more their ratio. We ran simulations with two wavelengths, $\lambda_{exc} = 313$ nm and $\lambda_{exc} = 254$ nm, that correspond to very different photoconversion rates: higher for the $trans \rightarrow cis$ isomerization at 313 nm, and for the $cis \rightarrow trans$ one at 254 nm. Table 4 shows the basic optical and kinetic data. The excitation,

photoconversion and energy absorption rates are all computed for isotropic conditions. In particular, the maximum absorbed power W is given for the isomer with the higher absorption coefficient. In the worst case $W = 4.5$ kcal mol^{-1} ps^{-1}, or twice this value with $F = 20$ GW/cm^2, which is the largest irradiance we tried. This means that the concentration of azobenzene should be at most 10^{-4} M, to ensure that heating is negligible after 1000 ps of irradiation.

Figure S3 shows the time dependence of the *cis* isomeric fraction F_{CAB}, with a long light pulse. In all cases, F_{CAB} is a monotonous function of time tending to a constant asymptote. Of course, the net *trans* → *cis* isomerization rate is higher with $\lambda_{exc} = 313$ nm than with 254 nm. As in normal reversible photochemistry without competition by thermal reactions, higher irradiances just accelerate the process, without affecting the photostationary state to a good approximation. However, one can notice a small decrease in the asymptotic values of F_{CAB} as the irradiance increases (see Table 5 for numeric data). This is due to the anisotropy, that is more pronounced at higher irradiances, resulting in a weaker absorption rate with respect to the isotropic case. Since TAB

Table 4: Optical and kinetic data for the irradiance $F = 10$ GW/cm^2 and two excitation wavelengths.

	$\lambda_{exc} = 313$ nm	$\lambda_{exc} = 254$ nm
ε_{TAB}, M^{-1} cm^{-1}	22020	2450
ε_{CAB}, M^{-1} cm^{-1}	2940	6900
TAB excitation rate, ps^{-1}	0.044	0.005
CAB excitation rate, ps^{-1}	0.006	0.017
$\frac{trans \to cis}{cis \to trans}$ conversion rate ratio	3.23	0.12
maximum absorbed power, kcal mol^{-1} ps^{-1}	4.50	1.92

Table 5: Photostationary state in different conditions. Final times t_f in ps, wavelengths λ_{exc} in nm, irradiances F in GW/cm^2.

| type of run	λ_{exc}	F	t_f	F_{TAB}	F_{CAB}	R_{TAB}	R_{CAB}	R_{tot}
regular	313	5	2000	0.259	0.741	-0.049	-0.005	-0.038
regular	313	10	1000	0.266	0.734	-0.067	-0.013	-0.052
regular	313	20	1000	0.275	0.725	-0.091	-0.032	-0.075
no isom.	313	10	1000	1.000	0.000	-0.068	—	-0.068
regular	254	10	1000	0.891	0.109	-0.032	-0.015	-0.027
no isom.	254	10	1000	1.000	0.000	-0.027	—	-0.027

Figure 5: Dichroic ratios as functions of time, with $\lambda_{exc} = 313$ nm and 254 nm, long irradiation.
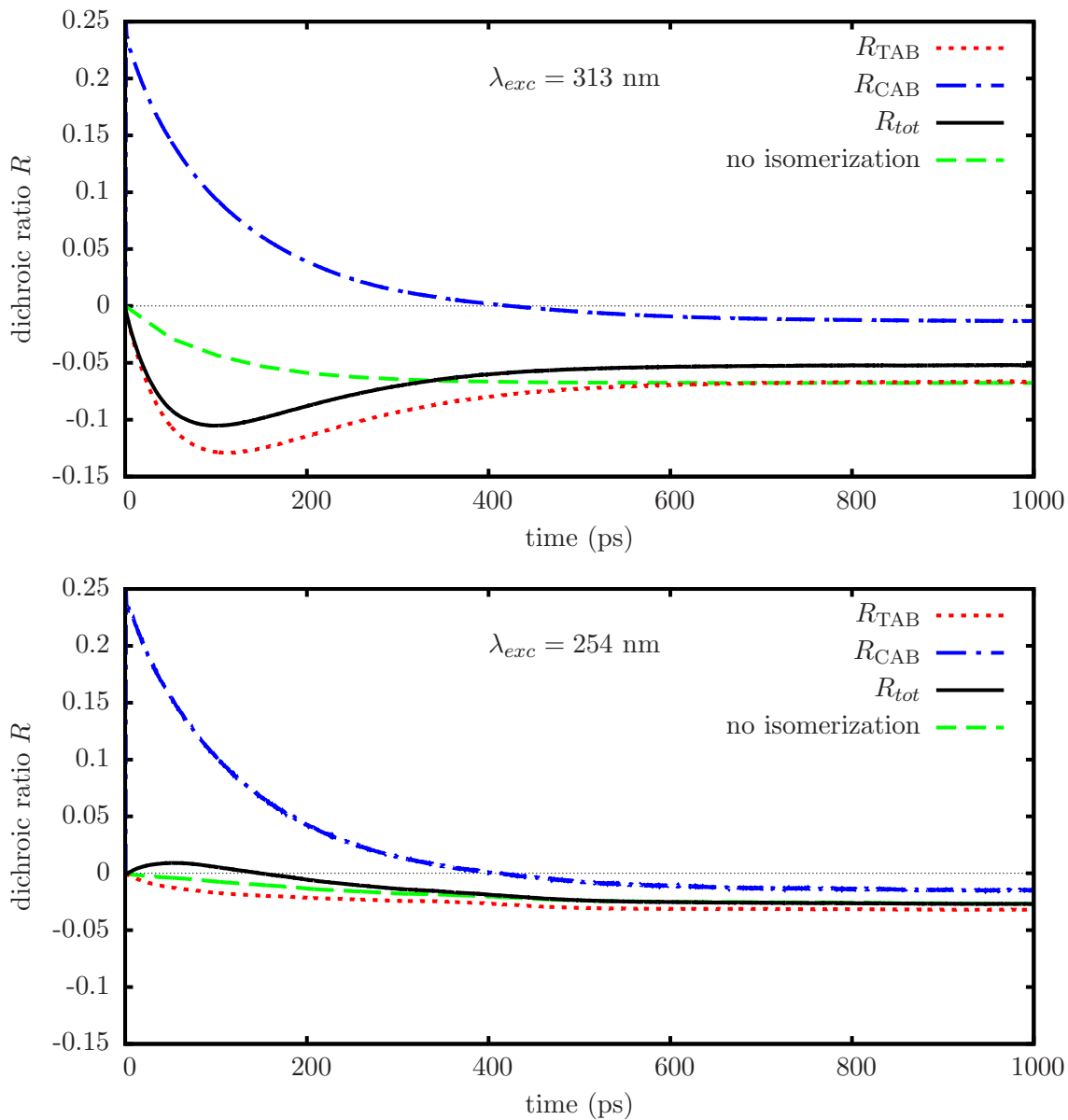
is more anisotropic than CAB, for reasons we shall see later, the $trans \rightarrow cis$ photoisomerization rate is more affected than the $cis \rightarrow trans$ one. With a 100 ps pulse, the F_{CAB} value just remains constant after $t = 100$ ps, because the thermal $cis \rightarrow trans$ conversion rate is negligible in this context and we have not taken into account this process.

16

Figure 6: Reduced densities as functions of the β and γ angles, from the simulations with $F = 10$ GW/cm^2, at $t = 100$ ps.
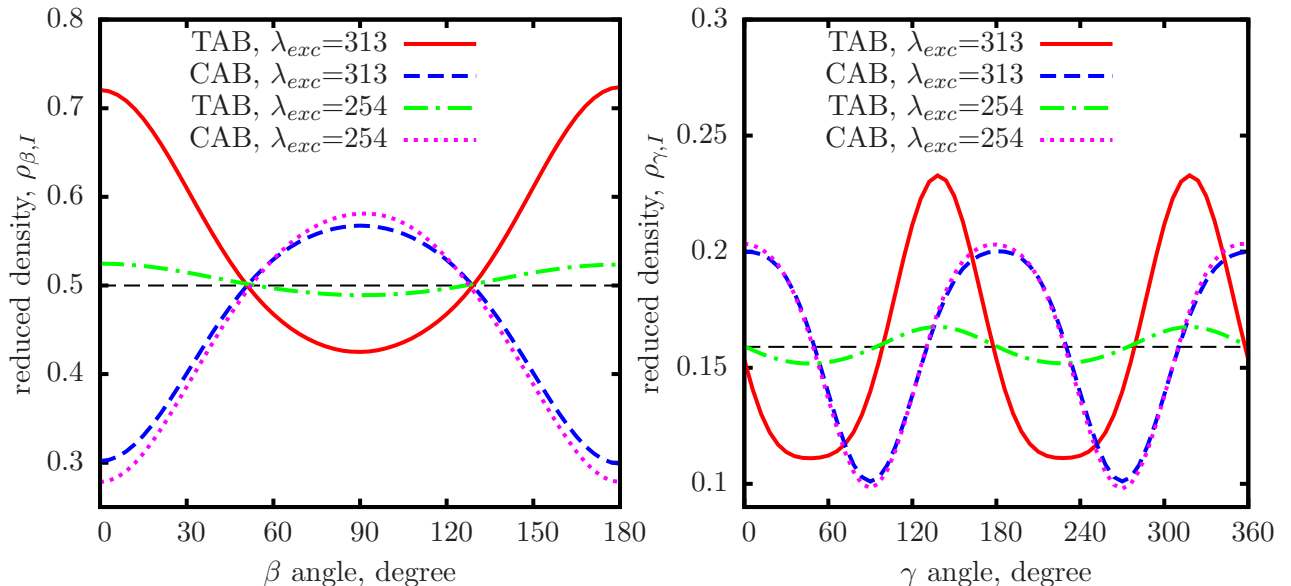
In Figure 5 we plot the dichroic ratios as functions of time, with $F = 10$ GW/cm^2. Similar results for $F = 5$ and 20 GW/cm^2 are shown in Figure S4. The two most prominent features are that the contributions of the two isomers to the dichroic ratio are of opposite sign for long intervals of time, and that the dichroic ratios are not necessarily monotonous functions of time. More detailed information about the anisotropy is contained in the full and reduced density functions: in Figure 6 we display $\rho_{\beta,I}$ and $\rho_{\gamma,I}$ at $t = 100$ ps, a time where R_{tot} is close to its maximum in the simulation with $\lambda_{exc} = 313$ nm and $F = 10$ GW/cm^2. Note that α is the rotation angle of a molecule around the lab axis $\hat{Z}$. Since the light is $\hat{Z}$-polarized, the problem is cylindrically symmetric around the $\hat{Z}$ axis, so no anisotropy is developed as a function of α, and this is why we only plot $\rho_{\beta,I}$ and $\rho_{\gamma,I}$. To understand the results of Figures 5, 6 and S4, we can start with a generally accepted mechanism [1–3, 9–11, 18–21]: molecules with large projections $\mu_{0,n,Z}$ of the transition dipole on the light polarization axis (here $\hat{Z}$) enjoy higher excitation rates than those with small $\mu_{0,n,Z}$. Therefore a net transfer of population occurs from the orientations Ω corresponding to large $\mu_{0,n,Z}$ to those with small $\mu_{0,n,Z}$, counteracted and eventually balanced by rotational diffusion. The dichroic ratio measured at $\lambda_{probe} = \lambda_{exc}$ must then be negative. This mechanism seems to describe adequately the effect of unreactive events. Many authors underline that, with a similar mechanism,

17

photoisomerization must boost the development of anisotropy, because it is likely to cause larger reorientations [1–3, 9–11]. A formal analysis of several hypothetical models including photoisomerization was offered by Dumont [19]. As we shall see, actually photoisomerization can play different roles: we start by noting that, while the starting isomer (TAB) exhibits a negative dichroic ratio at all times, R_{CAB} stays at positive values for few to several hundreds of ps.

A deeper insight can be gained by discussing the β and γ distributions. β is the angle between the $\hat{z}$ and the $\hat{Z}$ axes. At the equilibrium geometries of both isomers, all the $\pi \to \pi^*$ transition dipoles are orthogonal to the $\hat{z}$ axis, with the exception of the weak $S_0 \to S_2$ transition of CAB. Therefore, at β close to $0°$ or $180°$ ("high latitudes") we find low excitation rates, while near $\beta = 90°$ ("low latitudes") the rates are in the average higher. Within each isomer, i.e. considering the unreactive events only, this gradient of excitation rates results in a migration of molecules from low to high latitudes. For the same reason, the molecules with β far from $0°$ or $180°$ tend to rotate around the $\hat{z}$ axis (γ angle) so as to orient the transition dipole perpendicular to the light polarization: for TAB, this means $\gamma \simeq 135°$ or $315°$, while CAB should prefer $\gamma = 0°$ or $180°$. In Figure 6 we see that both the β and the γ distributions of TAB conform to this description, while those of CAB plainly contradict it.

To fully understand the simulation results, we must consider three processes that affect the orientational distribution of each isomer: unreactive photoexcitations (UP), i.e. photocycles going back to the initial isomer; reactive photoexcitations (RP), i.e. successful photoisomerizations; and ground state rotational diffusion (RD). As already discussed, the UP process tends to transfer population from orientations where the transition dipole components $\mu_{0,n,Z}$ are large to those where they are smaller, within each isomer; RD, of course, counteracts the building up of any kind of anisotropy. RP affects the anisotropy of both isomers, the reagent and the product of the photoisomerization. As we have seen at the end of section 4, even in the case of reactive events, small changes of the (unsigned) direction of the most important transition dipoles are more likely than large changes (here the boundary between "small" and "large" can be assumed to be the magic angle $\theta_m \simeq 54.7°$, such that $P_2(\theta_m) = 0$). Therefore, the TAB molecules that photoisomerize, having in most cases large $\mu_{0,n,Z}$ components, produce a CAB population with $R_{\mathrm{CAB}} > 0$ and a distribution of orientations with maxima at $\beta = 90°$ and $\gamma = 0°$ or $180°$. This effect of the RP process prevails at short times, because all the CAB molecules

have been freshly produced by photoisomerization. RP also contributes to the increase of $|R_{\mathrm{TAB}}|$, by selectively removing from the TAB population the molecules with large $\mu_{0,n,Z}$. If we compare $\rho_{\beta,I}$ and $\rho_{\gamma,I}$ obtained with $\lambda_{exc} = 313$ or 254 nm, we see that the CAB densities are quite similar, while in the case of TAB the maxima and minima appear at the same angles but are much more pronounced with $\lambda_{exc} = 313$ nm. The different behaviour of the two isomers is due to the fact that the CAB population is generated by the RP process and is anisotropic since the very beginning, while the TAB one is initially isotropic and the development of its anisotropy depends on the absorption rate.

As the CAB population builds up, its own UP process gains importance, so its dichroic ratio decreases and becomes eventually negative. Of course, also the $cis \rightarrow trans$ photoisomerization rate increases in time, and its effect on the anisotropy is similar to that of the $trans \rightarrow cis$ conversion, but opposite in sign: i.e. it gives a positive contribution to R_{TAB} and a negative one to R_{CAB}. Summarizing, when the two isomers coexist, the dichroic ratio of each of them is pushed towards (more) negative values by its own UP and RP processes and in the opposite direction by the RP process originated by the other isomer. Of course RD always tends to decrease in module the dichroic ratios. The effectiveness of the opposite UP and RP contributions depends, among other factors, on the relative abundance of the two isomers. So, as $F_{\mathrm{CAB}}/F_{\mathrm{TAB}}$ steadily increases, R_{TAB} is more and more influenced by CAB's RP, and after going through a negative minimum can decrease in absolute value. This behaviour is actually observed with $\lambda_{exc} = 313$ nm, but not with $\lambda_{exc} = 254$ nm, because in the latter case the fraction of CAB increases more slowly and remains lower.

At the photostationary state, the rates of $trans \rightarrow cis$ and $cis \rightarrow trans$ photoconversion are equal, i.e.

$$A_{\mathrm{TAB}} \; \Phi_{\mathrm{TAB} \rightarrow \mathrm{TAB}} = A_{\mathrm{CAB}} \; \Phi_{\mathrm{CAB} \rightarrow \mathrm{TAB}} \tag{18}$$

where A_I is the absorption rate of isomer I. Then, the RP processes starting from TAB and from CAB create anisotropy of the other isomer approximately at the same rate, and the less abundant isomer tends to be more affected by the photoisomerization of the other one: of course, the isomeric ratios depend on λ_{exc}. On the contrary, the UP mechanism is always more effective for TAB than for CAB, because of the different quantum yields. The rates of unreactive

Figure 7: Dichroic ratios as functions of time, with $\lambda_{exc} = 313$ nm and $F = 10$ GW/cm^2, 100 ps irradiation.
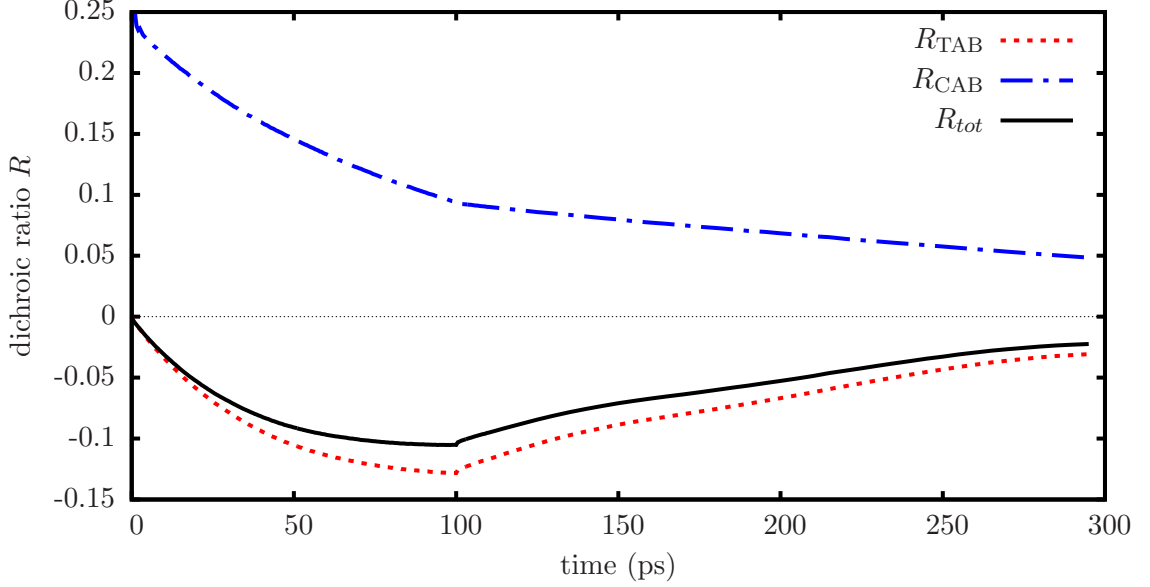
events, U_{TAB} and U_{CAB}, are in a fixed ratio at the photostationary state:

$$\frac{U_{\text{TAB}}}{U_{\text{CAB}}} = \frac{A_{\text{TAB}}\left(1 - \Phi_{\text{TAB}\to\text{TAB}}\right)}{A_{\text{CAB}}\left(1 - \Phi_{\text{CAB}\to\text{TAB}}\right)} = \frac{\Phi_{\text{CAB}\to\text{TAB}}\left(1 - \Phi_{\text{TAB}\to\text{TAB}}\right)}{\Phi_{\text{TAB}\to\text{TAB}}\left(1 - \Phi_{\text{CAB}\to\text{TAB}}\right)} \simeq 3.9 \quad (19)$$

This large ratio explains why, in the asymptotic region of all simulations, TAB is more anisotropic than CAB.

In order to highlight the relative importance of the UP and RP processes in the development of anisotropy, we also ran two simulations in which the photoisomerization was suppressed. The time-dependent dichroic ratios are shown in Figure 5 and the asymptotic values are listed in Table 5. We see that the increase of $|R_{\text{TAB}}|$ is slower in the absence of photoisomerization than in the regular simulation, because the $trans \to cis$ RP contribution is missing. However, the difference decreases in the long run, when the $cis \to trans$ RP mechanism tends to balance the $trans \to cis$ one in the regular runs. At $\lambda_{exc} = 313$, the asymptotic $|R_{tot}|$ is even larger without than with photoisomerization.

Finally, we present a simulated experiment performed with a 100 ps light pulse, $\lambda_{exc} = 313$ nm and $F = 10$ GW/cm^2 (see Figure 7). Up to 100 ps the results are identical to those obtained with the long irradiation time, same

λ_{exc} and irradiance. After 100 ps, the R_{TAB} and R_{CAB} dichroic ratios decay in time due to the rotational diffusion. Both functions are very well fitted by exponentials, with time constants of 150 ps for TAB and 310 ps for CAB. We see that these times are of the same order of magnitude as the longest ones (τ_3) obtained for the three-exponential fit of the autocorrelation functions relative to the rotational diffusion (see Table 2). The shorter time constants concerning the $\langle P_{2,n} \rangle$ functions, most relevant to the present discussion, are $\tau_1 \ll 1$ ps, and τ_2 roughly in the range 10-40 ps. There are two reasons why the τ_1 and τ_2 times have little relevance as to the decay of the dichroic ratios. The first reason mainly applies to τ_1, and is that a very fast but partial decay of the autocorrelation is already discounted when the irradiation stops at 100 ps, because most molecules have been excited for the last time several ps earlier. Note that a very small but fast decrease of $|R_{\mathrm{TAB}}|$ can however be noticed in Figure 7; anyway, such a feature would be irrelevant in a more realistic simulation, with a smoothly switched off light pulse. The main reason why we do not observe a component of the R_{TAB} or R_{CAB} decay with a time constant in the range of few tens of ps, as the τ_2 times of Table 2, lies in the kind of molecular motions that are involved. In fact, as discussed in section 3, both the pedalling motion of TAB and the overall rotation of CAB around the $\hat{n}_{ph-ph}$ axis leave almost unchanged the orientation of the most important transition dipoles, which is why they do not contribute to the decay of the optical anisotropy. However, other simulation results show that RD is not a simple first-order process, as already apparent from the autocorrelation functions of the molecular axes discussed in section 3. In fact, the asymptotic R_I values increase less than proportionally to the irradiance F (see Table 2), indicating that the RD efficiency is higher in the short time range.

6   Conclusions.

This paper presents simulations of the development of anisotropy in a dilute solution of azobenzene in ethylene glycol, subjected to linearly polarized light. Most experimental tests of potential technological interest were performed on systems in which the chromophores interact with each other, to take advantage of the mesogenic properties of the azo-compounds [1–13]. However, we feel that some new findings described in this work are of general interest, even beyond the specific case of azobenzene. Ethylene glycol is a solvent of moderate viscosity at room temperature, so we find rotational diffusion times of

azobenzene in the order of 100 ps. As a consequence, high irradiances are needed to obtain a sizeable anisotropy (we ran most tests with 10 GW/cm^2). Matrices that slow down more drastically the thermal rotation would require lower irradiances for longer times, getting closer to practical exploitability.

Our simulations are based on a stochastic model [14] and make use of statistical distributions of the reorientation of the molecular frame, due to ground state rotational diffusion or to the photochemical cycle (excitation, decay and possibly isomerization). Such distributions were obtained by computing the thermal and photochemical molecular dynamics of a single azobenzene molecule in a cluster of solvent [15], which is a novelty with respect to previous work based on parameterized models of reorientation [17–21]. We find that the internal motions, in particular the "pedalling" of *trans*-azobenzene (simultaneous torsion of both N-C bonds), reduce the rotational diffusion times and determine a multi-exponential decay of the autocorrelation functions of the molecular axes. We confirm that the photochemical cycle is more effective in promoting the reorientation of both isomers, i.e. it causes larger rotations of the molecular frame, than the thermal dynamics in a comparable interval of time. However, if we concentrate on the most important transition dipole moments, we find that the memory of the initial orientation is partially conserved not only in the unreactive photocycles (excitation and decay without isomerization), but even after the photoisomerization.

We computed dichroic ratios for each isomer I (R_I) and for the whole sample (R_{tot}), relative to the absorption of probe pulses polarized either parallel or perpendicular to the exciting light. The probe light was assumed to be of the same wavelength as the exciting one, but the physical effects we have highlighted would be relevant also with more complex experimental setups. The simulations show that the anisotropy of a given isomer I is affected by three processes: unreactive photochemical events, that tend to orient the most important transition dipoles $\vec{\mu}_{0,n}$ perpendicular to the polarization of the light ($\hat{Z}$ axis), thus yielding a negative contribution to the dichroic ratio R_I; photoisomerizations, of which those starting from isomer I also drive R_I toward (more) negative values, while those starting from the other isomer have the opposite effect; and rotational diffusion, that tends to decrease R_I in module, whatever its sign. As a result of these contrasting effects, the dichroic ratios of the two isomers may have opposite signs, especially at the beginning of the irradiation; and R_{tot}, as well each of the R_I's, can be non-monotonic functions of time. This means that a longer irradiation will not always yield a more pro-

nounced anisotropy. We also show that isomerization is strongly coupled with the development of anisotropy, but is not a necessary ingredient, as commonly assumed: simulations in which photoisomerization was artificially suppressed yielded anisotropies in the same range as the regular ones. Therefore, matrices in which the photoisomerization is completely or almost suppressed, or chromophores that do not isomerize, should not be discarded as candidates for photoinduced anisotropy studies and applications.

7   Appendix A.

In this Appendix we specify the body fixed frame for the azobenzene molecule. We only consider four atoms, namely the C′-N′=N″-C″ group. The definition of the body fixed frame applies to any geometrical arrangement, except when all four atoms are collinear. However, we are particularly interested in geometries close to the *cis* and *trans* minima (CAB and TAB). The definitions of the axes are as follows (see also fig. 8):

(1) The $\hat{x}$ axis coincides with the N′-N″ one, i.e. it is obtained by normalizing the $\vec{R}_{\mathrm{N'N''}} = \vec{R}_{\mathrm{N''}} - \vec{R}_{\mathrm{N'}}$ vector.

(2) We determine the $\vec{A}$ vector by orthogonalizing $\vec{R}_{\mathrm{N'C'}}$ with respect to $\hat{x}$ and by subsequent normalization.

(3) Similarly, we determine $\vec{B}$ by orthogonalizing $\vec{R}_{\mathrm{N''C''}}$ with respect to $\hat{x}$ and by normalizing it.

(4) We calculate $\vec{C} = \vec{A} + \vec{B}$.

(5) We calculate $\vec{C}' = \hat{x} \wedge (\vec{B} - \vec{A})$.

(6) The direction of the $\hat{z}$ axis is taken along $\vec{C}$ or $\vec{C}'$, choosing the one with the larger norm. We have $C > C'$ at cisoid geometries ($-\pi/2 <$ ∠CNNC$< \pi/2$), and $C < C'$ at the transoid ones.

(7) Obviously $\hat{y} = \hat{z} \wedge \hat{x}$.

The reason for defining both $\vec{C}$ and $\vec{C}'$ and choosing the longer one is that $\vec{C}$ vanishes at the *trans* geometry ($\vec{A} = -\vec{B}$ for $\theta =$ ∠CNNC $= 180°$), while $\vec{C}'$ vanishes at the *cis* geometry with $\theta{=}0$ ($\vec{A} = \vec{B}$ for ∠CNNC $= 0$). Starting from TAB, θ may decrease from 180° to 0°, so that the molecule goes through the intermediate transoid and cisoid geometries of fig. 8. In this case, one switches smoothly from the definition based on the $\vec{C}'$ vector to that based on the $\vec{C}$ one, when θ drops below 90°. If, on the opposite, θ increases towards 360°, we obtain a capsized CAB, with the $\hat{z}$ and $\hat{y}$ axes pointing in opposite

Figure 8: Definition of the body-fixed frame. θ is the CNNC dihedral angle.
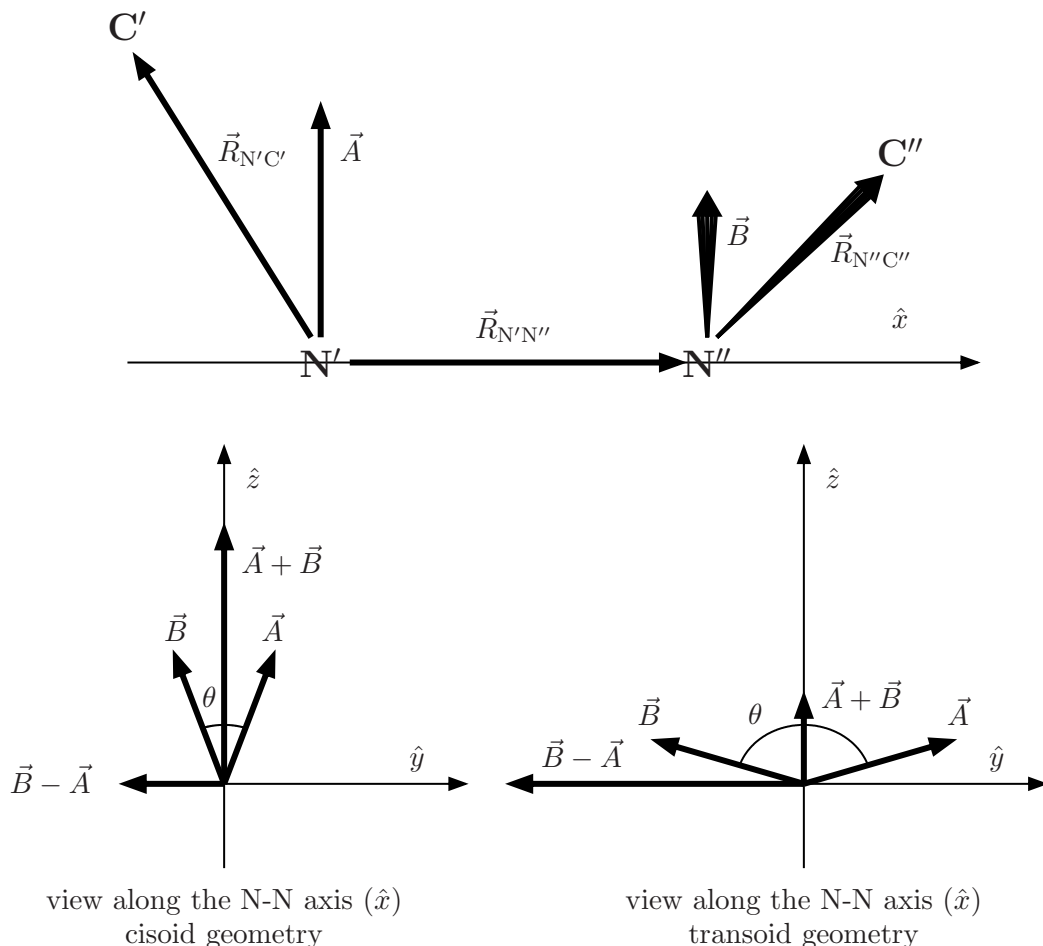
directions with respect to the former case. Note that, along this pathway, the definition of the frame changes suddenly at $\theta = 270°$.

Of course the two pathways have the same probability to occur. This is why the plots of the final $\hat{y}$ and $\hat{z}$ axes show an approximate inversion symmetry: the same density of points is found for a given pair of cartesian components and for the same with opposite signs. Of course the symmetry would be exact only in the large number limit (infinite trajectories), but one can easily symmetrize the distribution: for each reactive trajectory yielding CAB with a given orientation, we added one with reversed $\hat{z}$ and $\hat{y}$ axes. The same was done for the CAB$\rightarrow$TAB trajectories.

Acknowledgments

References

[1] C. Cojocariu and P. Rochon, *Pure Appl. Chem.*, 2004, **76**, 1479.

[2] K. G. Yager and C. J. Barrett, *J. Photochem. Photobiol. A*, 2006, **182**, 250.

[3] P. Camorani and M. P. Fontana, *Phys. Rev. E*, 2006, **73**, 011703.

[4] I. Vecchi, A. Arcioni, C. Bacchiocchi, G. Tiberio, P. Zanirato and C. Zannoni, *J. Phys. Chem. B*, 2007, **111**, 3355.

[5] T. Yoshino, M. Kondo, J. Mamiya, M. Kinoshita, Y. Yu and T. Ikeda, *Adv. Mater.*, 2010, **22**, 1361.

[6] M. Ji, Y. Li, T. White, A. Urbas and Q. Li, *Chem. Commun.*, 2010, **46**, 3463.

[7] J. Ma, Y. Li, T. White, A. Urbas and Q. Li, *Chem. Commun.*, 2010, **46**, 3463.

[8] D. Bléger, Z. Yu, and S. Hecht, *Chem. Commun.*, 2011, **47**, 12260.

[9] D. Rais, Y. Zakrevskyy, J. Stumpe, S. Nešpøurek and Z. Sedláková, *Opt. Mater.*, 2008, **30**, 1335.

[10] K. Oki and Y. Nagasaka, *Coll. Surf. A: Physicochem. Eng. Asp.*, 2009, **333**, 182.

[11] G. J. Fang, J. E. Maclennan, Y. Yi, M. A. Glaser, M. Farrow, E. Korblova, D. M. Walba, T. E. Furtak and N. A. Clark, *Nat. Commun.*, 2013, **4**, 1521.

[12] A. V. Bogdanov and A. Kh. Vorobiev, *J. Phys. Chem. B*, 2013, **117**, 12328.

[13] A. V. Bogdanov and A. Kh. Vorobiev, *J. Phys. Chem. B*, 2013, **117**, 13936.

[14] V. Cantatore, G. Granucci and M. Persico, *J. Comput. Chem.*, 2012, **33**, 1015.

[15] V. Cantatore, G. Granucci and M. Persico, *Comput. Theor. Chem.*, 2014, **1040**, 126.

[16] T. Cusati, G. Granucci, E. Martínez-Núñez, F. Martini, M. Persico and S. Vázquez, *J. Phys. Chem. A*, 2012, **116**, 98.

[17] Z. Sekkat, *Opt. Comm.*, 2004, **229**, 291.

[18] M. Dumont, *J. Opt. Soc. Am. B*, 2009, **26**, 1057.

[19] M. Dumont, *J. Opt. Soc. Am. B*, 2011, **28**, 1855.

[20] M. Persico and P. Van Leuven, *Phys. Chem. Chem. Phys.*, 2009, **11**, 8433.

[21] P. Van Leuven, V. Cantatore and M. Persico, *Phys. Chem. Chem. Phys.*, 2012, **14**, 1957.

[22] M. Böckmann, D. Marx, C. Peter, L. Delle Site, K. Kremer and N. L. Doltsinis, *Phys. Chem. Chem. Phys*, 2011, **13**, 7604.

[23] R. N. Zare, *Angular Momentum: Understanding Spatial Aspects in Chemistry and Physics*, J. Wiley (1988)

[24] T. Cusati, G. Granucci, M. Persico and G. Spighi,, *J. Chem. Phys.*, 2008, **128**, 194312.

[25] T. Cusati, G. Granucci, M. Persico *J. Am. Chem. Soc.*, 2011, **133**, 5109.

[26] M. Persico, G. Granucci, S. Inglese, T. Laino and A. Toniolo, *J. Mol. Struct. THEOCHEM*, 2003, **621**, 119.

[27] Eq. (13) was erroneously written in ref. [14] (where it is numbered as eq. (27)), by omitting the factors $F_I \langle A_I \rangle_{iso}$ in the weights. It was however correctly implemented in the calculations.

V. Cantatore, G. Granucci, M. Persico
The photo-orientation of azobenzene in viscous solutions, simulated by a
stochastic model.

Supplementary information.

Figure S1: Autocorrelation functions of the molecular axes $\langle P_{1,n} \rangle (t) = \langle \hat{n}(t_0) \cdot \hat{n}(t_0 + t) \rangle$, obtained by averaging over t_0 the results of the ground state dynamics of TAB and CAB in ethylene glycol.
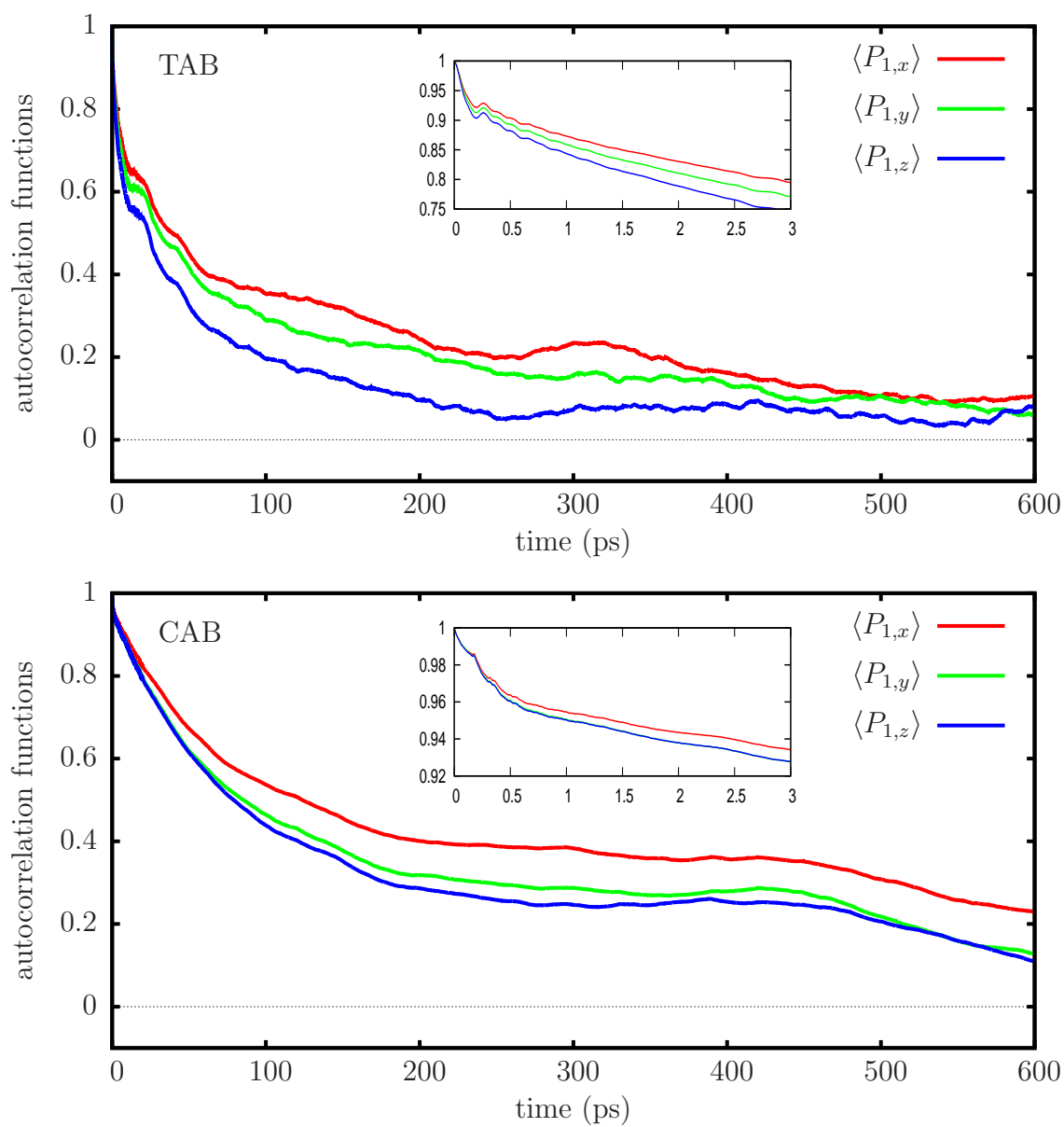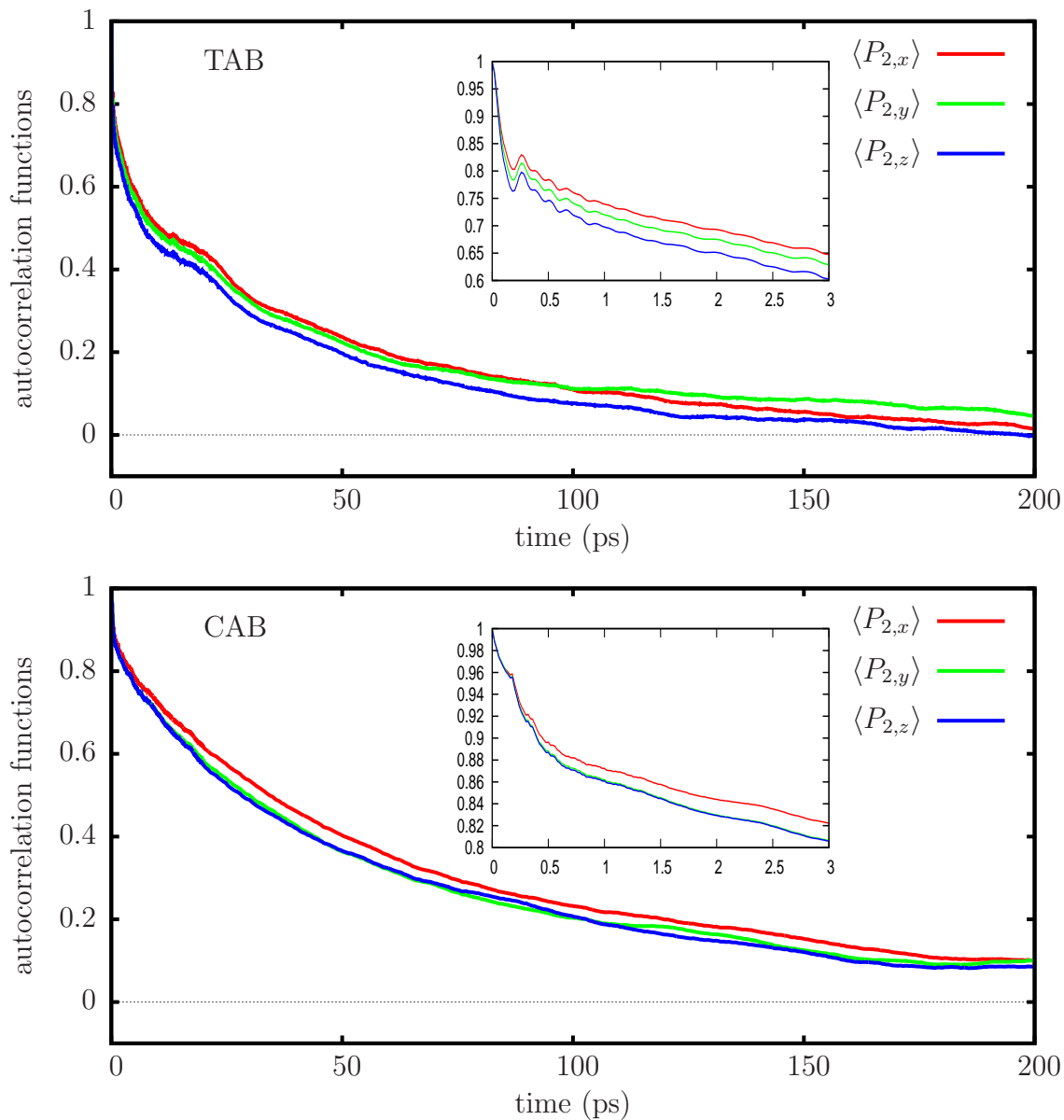
Figure S2: Autocorrelation functions of the molecular axes $\langle P_{2,n} \rangle (t) = \frac{1}{2} \langle 3[\hat{n}(t_0) \cdot \hat{n}(t_0 + t)]^2 - 1 \rangle$, obtained by averaging over t_0 the results of the ground state dynamics of TAB and CAB in ethylene glycol.

Figure S3: Isomeric fraction of CAB as a function of time. Wavelengths λ_{exc} in nm, irradiances F in GW/cm^2.
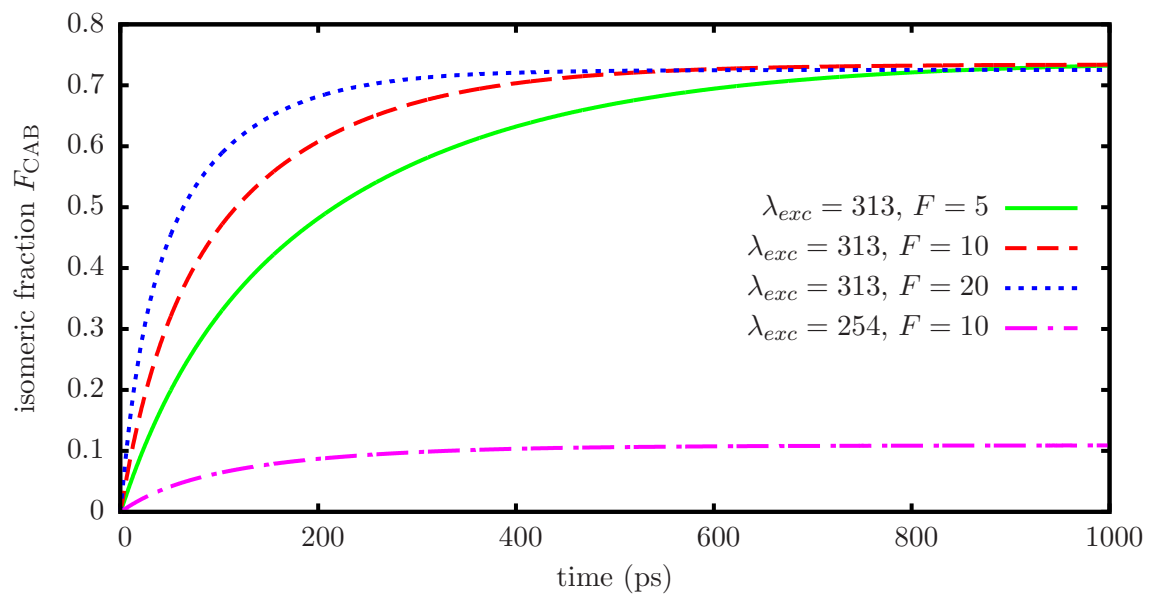
Figure S4: Dichroic ratios as functions of time, with $\lambda_{exc} = 313$ nm and two different values of irradiance.